

EE4620 Spectral Domain Methods in EM

Lecture notes:

Artificial Dielectrics

Outline

1. General Definition of Artificial Dielectrics
 - 1.1 Real Dielectrics
 - 1.2 Artificial Dielectrics: Main Properties
 - 1.3 Advantages of Artificial Dielectrics Layers and Application to Antennas
2. Analysis of Artificial Dielectric Layers
 - 2.1 Single Layer
 - 2.2 Multiple Layers
 - 2.3 Shift between Layers
3. Near Source Excitation
 - 3.1 Radiation Patterns
 - 3.2 Dispersion Analysis
4. Homogenization
 - 4.1 Parameter retrieval
 - 4.2 Design tool

1 General Definition of Artificial Dielectrics

1.1 Real Dielectrics

To better understand the basics of artificial dielectrics, we shall first remind how normal dielectric materials operate. A dielectric is a material composed by atoms in which electrons are strongly bound to the nucleus. A schematic representation of these atoms is shown in Figure 1(a). In absence of an external electric field, the material is electrically neutral, i.e. the negative and positive charges in the atoms balance each other. When an external electric field (\mathbf{E}_{ext} in Figure 1(b)) is applied to the material, the positive and negative charges in the atoms experience an electric force associated with \mathbf{E}_{ext} . The electric field cannot move the electrons like in a conductor, because they are tightly bound to the atoms. However, the field can still deform the atoms because of the force experienced by the charges. This effect is referred to as polarization of the material.

More specifically, since the electric force is oriented in the same direction of the field ($\mathbf{F} = q\mathbf{E}$), the force will push the positive charge slightly in the same direction of the vector \mathbf{E}_{ext} , while the negative charge will be pushed in the direction opposite to the field orientation. The resulting deformed atoms will have a non-negligible dipole moment, thus will behave as a small dipoles aligned with the external field. These dipoles produce a small electric field, called polarization field \mathbf{E}_{pol} , that opposes the external field, as shown in Figure 1(c) (recall that the electric field lines point outward for a positive charge and inward for a negative charge).

The total electric field can then be written as $\mathbf{E}_{\text{tot}} = \mathbf{E}_{\text{ext}} + \mathbf{E}_{\text{pol}}$ and, because \mathbf{E}_{pol} opposes \mathbf{E}_{ext} , we can also say that the total field is lower than the external field $E_{\text{tot}} < E_{\text{ext}}$. The factor by which the total field reduces compared to the external field is given by the relative permittivity: $\epsilon_r = E_{\text{ext}}/E_{\text{tot}} > 1$.

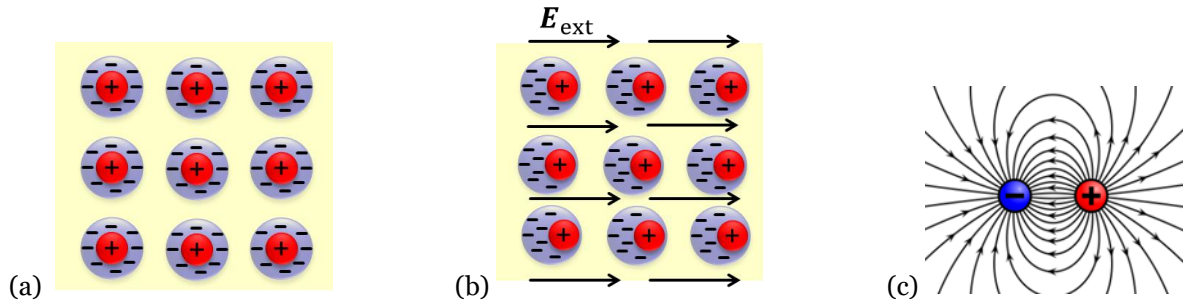


Figure 1: Atoms in a dielectric material (a) in absence and (b) in the presence of an external electric field E_{ext} . The external field deforms the atoms inducing a dipole moment: the atoms behave like (c) equivalent dipoles that produce an electric field in the opposite direction of the external field.

Besides the polarization field E_{pol} , we can also define the polarization vector \mathbf{P} as net electric dipole moment vector per unit volume. This vector is related to the electric flux density in vacuum by a constant χ_e called electric susceptibility:

$$\mathbf{P} = \epsilon_0 \chi_e \mathbf{E}. \quad (1)$$

We also know that the electric flux density in vacuum can be related to the electric field by

$$\mathbf{D} = \epsilon_0 \mathbf{E} \quad (\text{in vacuum}) \quad (2)$$

where ϵ_0 is the permittivity of vacuum. In a dielectric, the electric flux density can be written as the sum of the one in vacuum plus the polarization field due to the field generated by the deformed atoms:

$$\mathbf{D} = \epsilon_0 \mathbf{E} + \mathbf{P} \quad (\text{in dielectrics}). \quad (3)$$

By substituting (1) in (3), we can also express the electric flux density as

$$\mathbf{D} = \epsilon_0 \mathbf{E} + \mathbf{P} = \epsilon_0 \mathbf{E} + \epsilon_0 \chi_e \mathbf{E} = \epsilon_0 (1 + \chi_e) \mathbf{E} = \epsilon_0 \epsilon_r \mathbf{E} = \epsilon \mathbf{E} \quad (\text{in dielectrics}). \quad (4)$$

where we related the relative permittivity to the electric susceptibility as $\epsilon_r = 1 + \chi_e$, and the total permittivity is the product between vacuum permittivity and relative permittivity $\epsilon = \epsilon_0 \epsilon_r$. One important aspect to clarify is that when we write $\mathbf{D} = \epsilon \mathbf{E}$ or $\mathbf{D} = \epsilon_0 \mathbf{E} + \mathbf{P}$ we are referring to average quantities in the medium and not local quantities (point by point). In (3), \mathbf{E} is the average net field in the medium and \mathbf{P} is the average net dipole polarization per unit volume (dipole moment per unit volume). The local field in each point, at microscopic level, is much more complicate and does not follow the simple constitutive relation valid for the average field. For example, locally the field lines could look like the ones in Figure 2.

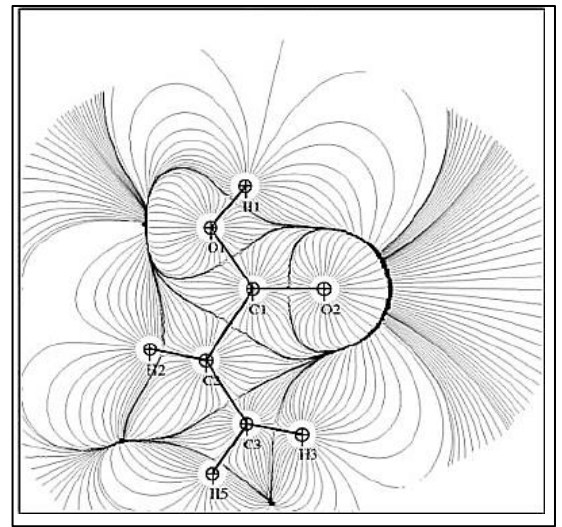


Figure 2: Local field $E(\mathbf{r})$ at microscopic level.

A dielectric is *isotropic* if it responds in the same way to an external field independently on the orientation of the field. In other words, the polarization of the dielectric is always aligned to the applied electric field and its magnitude is independent on the direction of the electric field. For

such a material, the flux \mathbf{D} and the field \mathbf{E} are always parallel. More general materials are *anisotropic*, i.e. their electromagnetic properties change with the direction of the fields. For such materials, the permittivity and permeability are not single numbers ϵ and μ , but they become tensors $\underline{\underline{\epsilon}}$ and $\underline{\underline{\mu}}$, to link each component (x,y,z) of the flux densities to each components (x,y,z) of the associated fields. The constitutive relations become

$$\mathbf{D} = \underline{\underline{\epsilon}}\mathbf{E} = \begin{bmatrix} \epsilon_{xx} & \epsilon_{xy} & \epsilon_{xz} \\ \epsilon_{yx} & \epsilon_{yy} & \epsilon_{yz} \\ \epsilon_{zx} & \epsilon_{zy} & \epsilon_{zz} \end{bmatrix} \mathbf{E} , \quad \mathbf{B} = \underline{\underline{\mu}}\mathbf{H} = \begin{bmatrix} \mu_{xx} & \mu_{xy} & \mu_{xz} \\ \mu_{yx} & \mu_{yy} & \mu_{yz} \\ \mu_{zx} & \mu_{zy} & \mu_{zz} \end{bmatrix} \mathbf{H} \quad (5)$$

thus the flux densities are not parallel to the fields (\mathbf{D} is not parallel to \mathbf{E} and \mathbf{B} is not parallel to \mathbf{H}).

1.2 Artificial Dielectrics: Main Properties

Artificial dielectrics (ADs) were introduced in the 1940's in [1] as a light-weight alternative to real dielectric materials, initially used to realize microwave lenses [2]. After their introduction, ADs have been extensively studied and used for decades for radar development. An AD consists of a large-scale model of an actual dielectric, obtained by embedding conducting structures in a host material according to a regular pattern. Some physical realizations of ADs involve the insertion of metallic spheres, cylinder and strips inside a dielectric in a periodic arrangement, as shown in Figure 3.

In all these scenarios, the electric field scattered by the metallic inclusions, when added to the incident field, creates an effective change in total field similarly to real dielectrics [3]. At the frequencies for which the periodicity of the pattern is much smaller than the wavelength, the structure can be assigned equivalent parameters that describe an homogeneous dielectric. The effective electric parameters can be engineered by varying the size of the metal obstacles and their spatial density.

In the case of spherically symmetric obstacles, as shown in Figure 3(a), the equivalent medium is isotropic, since the effect of the impressed field on the structure is independent of the polarization and the angle of incidence. However, other types of artificial dielectrics, such as the ones in Figure 3(b) and (c), have anisotropic properties: both the polarization and the angle of incidence of the external electric field have significant impact on the equivalent properties of the structure.

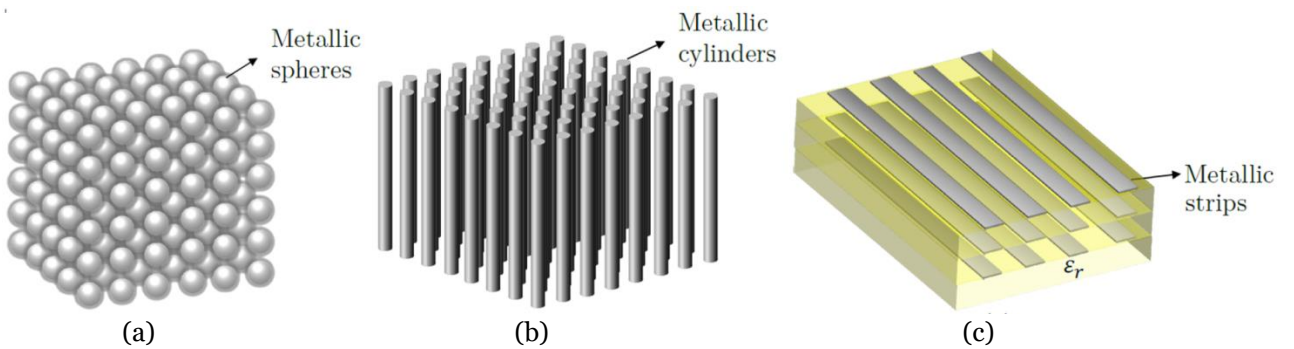


Figure 3. Artificial dielectric layer embedded in a host dielectric: three- dimensional (a) spheres and (b) cylinders, and (c) planar two-dimensional metallic strips.

In this course, a specific type of anisotropic AD is studied in detail, which is realized as a cascade of planar layers made of printed metal patches, as depicted in Figure 4. Such structures are also referred to as artificial dielectric layers (ADLs). ADLs consist of periodic metallic patches, small with respect to the wavelength (λ), embedded in a host material to realize an equivalent material with modified properties (Figure 4(a)). The equivalent electromagnetic parameters of the artificial material can be engineered by properly designing the metallic patches. Being anisotropic, the ADLs

are equivalent to a homogenous material that is characterized by an effective permittivity and permeability tensors $\underline{\underline{\epsilon}}_{\text{eff}}$ and $\underline{\underline{\mu}}_{\text{eff}}$ (Figure 4(b)). The effective refractive index of the equivalent material n_{eff} is higher than that of the medium hosting the patches n_{host} . Moreover, because of the anisotropy, the effective refractive index of a plane wave travelling through the material is a function of the angle of incidence θ and the polarization $\hat{\mathbf{p}}$ (orientation of the electric field) of the plane wave: $n_{\text{eff}}(\theta, \hat{\mathbf{p}})$. For example, the refractive index is different for transverse electric (TE) and transverse magnetic (TM) components of an incident plane wave.

Reminder: the refractive index is the ratio between the speed of wave in vacuum c divided by the phase velocity of the wave in the medium v_p : $n = c/v_p$. For a homogeneous isotropic dielectric, the refractive index is related to the relative permittivity and permeability $n = \sqrt{\epsilon_r \mu_r}$.

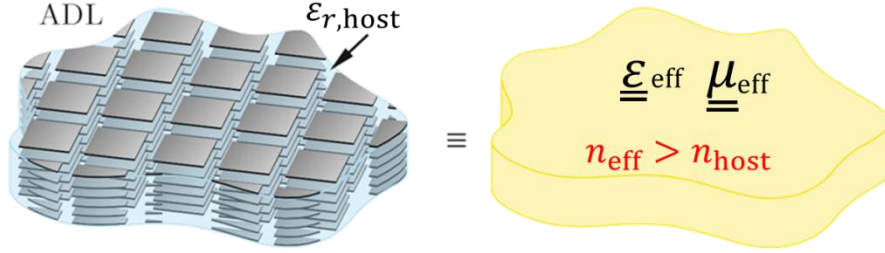


Figure 4. Artificial dielectric layers to realize an equivalent anisotropic material.

To understand the operation of artificial dielectrics, one can imagine an incident field \mathbf{e}_{inc} impinging on the periodic patches, as shown in Figure 5. To verify the boundary conditions, the incident field must induce electric currents \mathbf{j} on the metal that scatter a field $\mathbf{e}_{\text{scatt}}$. The condition $\hat{\mathbf{n}} \times \mathbf{e}_{\text{scatt}} = -\hat{\mathbf{n}} \times \mathbf{e}_{\text{inc}}$ must be verified on the metal so that the total tangential field $\hat{\mathbf{n}} \times \mathbf{e}_{\text{tot}}$ is 0. Thus, to ensure that the total tangential field is zero on the metal, the metal patches scatter a field that tends to oppose the incident field. As such, the metallic scatterers have a role similar to atoms or molecules in a real dielectric (Figure 1(b)).

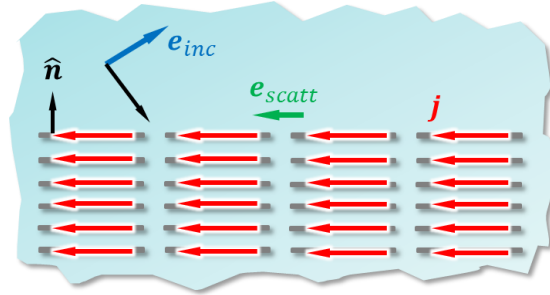


Figure 5. Field Picture in Artificial Dielectric Layers under plane wave incidence.

1.3 Advantages of Artificial Dielectric Layers and Application to Antennas

We have mentioned earlier that the effective refractive index of ADLs changes with the polarization and incidence angle of a plane wave. The specific dependence on these parameters is shown in Figure 6. If a plane wave impinges on the ADL structure with an angle of incidence θ , it ‘sees’ different refractive indexes, depending on the angle. More specifically, the refractive index is higher for normal incidence ($\theta = 0^\circ$) and becomes smaller and smaller for increasing angles. Moreover, the refractive index for TE and TM incidence are different. The one for TM tends to the refractive index of the hosting medium when $\theta = 90^\circ$ (grazing incidence), because for this angle the electric field is orthogonal to the patches and does not interact with them. The refractive index for the TE component tends to a higher value for $\theta = 90^\circ$, since the electric field is parallel to the patches and still interacts with them. Nevertheless, the important property is that for both polarizations, TE

and TM, the refractive index decreases with the angle; it is high for normal incidence and becomes lower and lower when moving to grazing incidence.

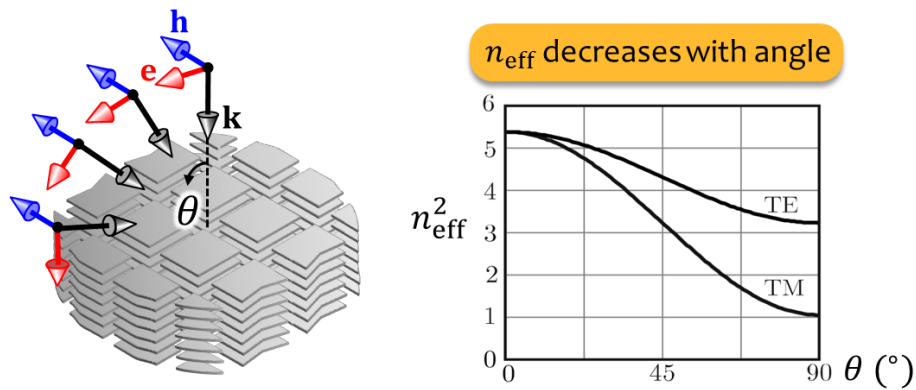


Figure 6. Variation of the effective refractive index of ADLs with angle of incidence and component of the plane wave. The hosting medium is air ($n_{\text{host}} = 1$) in this example.

This fundamental property has a great advantage for antenna applications, illustrated in Figure 7. A relevant parameter for antenna design is the so called front-to-back ratio, which is the ratio between the power radiated in a certain desired direction (front) and the one radiated in the opposite undesired direction (back). A small radiating element (e.g. a small dipole) tends to radiate equal power in both directions, thus it has a poor front-to-back ratio (equal to 1 or 0 dB). One typical way to improve the front-to-back ratio is to place a dielectric slab with high permittivity above the source. In this way, a larger portion of the radiated electromagnetic power tends to be drawn in the direction of the dense material, increasing the front-to-back ratio. However, only the power that is radiated vertically (vertical rays) manages to exit the dense material, while all the rays that arrive with an angle above the critical angle undergo total internal reflection at the top interface of the slab. These rays remain trapped in the dielectric slab and form surface waves, which are undesired because these are associated with power loss and reduced antenna efficiency.

However, due to the anisotropy, artificial dielectrics implement an angle-dependent effective refractive index. The vertical rays still see a high permittivity and thus the front-to-back ratio is increased similarly to a real dielectric. On the other hand, unlike real dielectrics, the rays that arrive at an angle see a lower refractive index, thus they never encounter the critical angle on the top interface of the ADL and they can be radiated out from the slab. Therefore, ADL can achieve high front-to-back ratio without supporting surface waves [4].

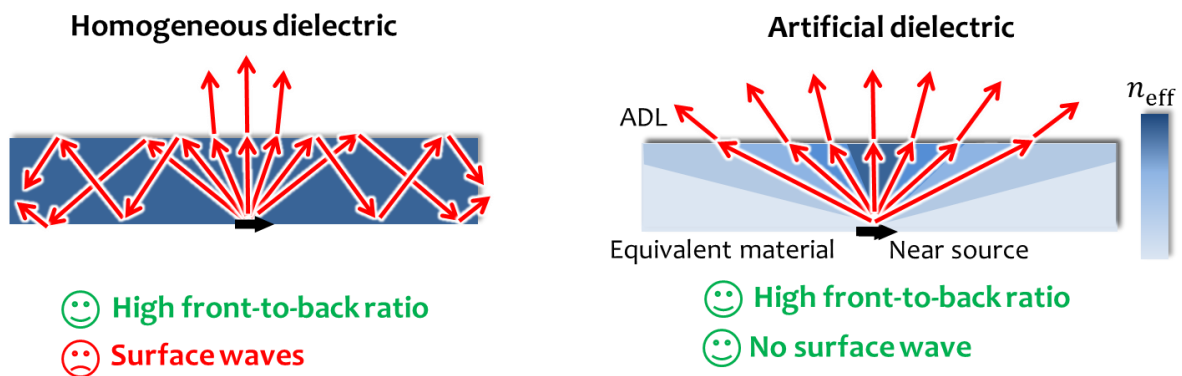


Figure 7. Advantages of artificial dielectrics with respect to real dielectrics.

This discovery has had a huge impact on antenna design. Since most known antennas are printed or integrated on dielectric slabs, surface waves have been the main issues of antenna designers for

decades. ADLs effectively solve this problem. Some successful examples of application of ADLs for enhancing antenna performance are:

- On-chip antennas [5]: High frequency on-chip antennas are characterized by poor radiation efficiency, because they are located only at around $10\mu\text{m}$ distance from a ground plane or from a very lossy silicon layer. Placing ADLs above the antenna enables high-efficiency radiation from chips.
- Wideband phased arrays [6]: ADLs can be placed above phased array antenna to improve matching bandwidth and scan range capability without supporting surface waves. This concept will be explained in detail in other lecture notes (connected arrays).

2 Analysis of Artificial Dielectric Layers

2.1 Single Layer

To explain the method used for the analysis of artificial dielectric layers, we first consider the simpler problem of a single layer of sub-wavelength periodic square patches in free space under generic plane-wave illumination [7]. The geometrical parameters are shown in Figure 8. The patches are assumed to be infinitely thin and perfectly conducting. A spectral method is derived for the solution and is described here.

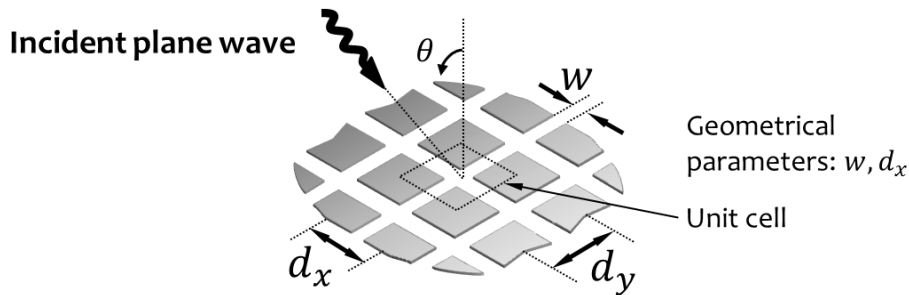


Figure 8. Single layer of sub-wavelength periodic square patches in free space under generic plane-wave illumination, with geometrical parameters.

Setting up the Integral Equation

The original problem is depicted in Figure 9(a), and represents a plane wave impinging on the layer unit cell. Note that the unit cell is centered on the junction of the slots (gaps between patches) rather than on the patch itself, as also shown in Figure 8.

The first step is to apply the equivalence theorem. We could decide to apply the equivalent current on the metal, leading to an electric field integral equation (EFIE), or on the gap (aperture formulation), leading to a magnetic field integral equation (MFIE). In this case, it is convenient to choose the latter option and solve the problem for the slots, which explains why unit cell is centered on the slots in the original problem. By applying the equivalence principle, a very thin surface surrounding the gap is considered, where equivalent magnetic and electric surface currents are defined. The fields inside the surface are arbitrary and can be assumed to be equal to 0 (this choice is known as Love's equivalence principle). Also, since the current in the Love's equivalence principle produce a null field inside the volume, the properties of the material within the surface are also arbitrary. Thus we can fill the volume inside the surface with metal (Figure 9(b)) without altering the solution outside. Being located on a metal sheet, only the magnetic currents \mathbf{m}_0 survive, while the electric currents do not contribute to radiation (they cancel out with their image).

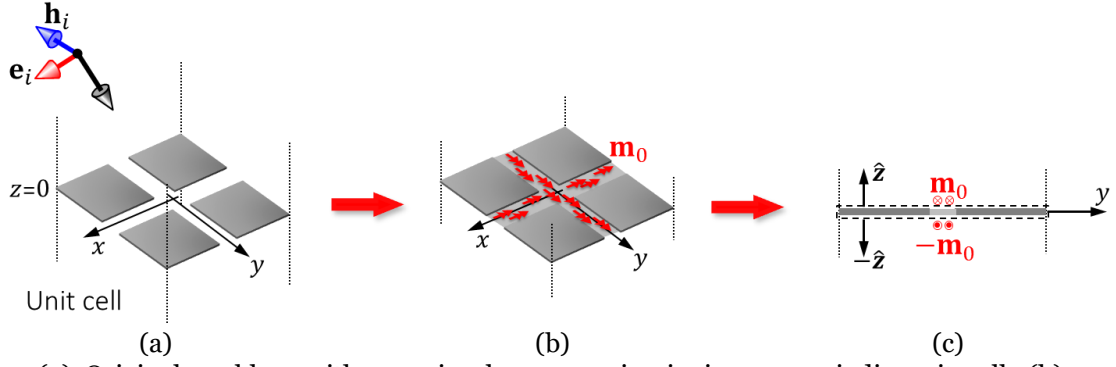


Figure 9. (a) Original problem with generic plane wave impinging on periodic unit cell; (b) equivalent problem with unknown magnetic current on the gaps, filled with metal; (c) equal and opposite magnetic currents above and below layer to satisfy continuity of electric field in the gap.

The surface magnetic currents must satisfy the boundary condition $\mathbf{m}_0 = \mathbf{e} \times \hat{\mathbf{n}}$, where $\hat{\mathbf{n}}$ is the outward unit vector normal to the surface. We can now impose the continuity of the electric field at $z = 0$, i.e. the electric field right above the gap \mathbf{e}^+ and right below the gap \mathbf{e}^- are equal: $\mathbf{e}^+ = \mathbf{e}^-$. Therefore, the magnetic currents above and below the gap

$$\begin{aligned} \mathbf{m}_0^+ &= \mathbf{e}^+ \times \hat{\mathbf{n}} = \mathbf{e}^+ \times \hat{\mathbf{z}} \\ \mathbf{m}_0^- &= \mathbf{e}^- \times \hat{\mathbf{n}} = \mathbf{e}^- \times (-\hat{\mathbf{z}}) \end{aligned} \quad (6)$$

must be equal and opposite: $\mathbf{m}_0^+ = -\mathbf{m}_0^- = \mathbf{m}_0$, as in Figure 9(c).

The last step to write the integral equation is to impose the continuity of the magnetic field at $z = 0$ ($\mathbf{h}^+ = \mathbf{h}^-$). The magnetic field above \mathbf{h}^+ is the sum of the incident magnetic field \mathbf{h}_i , plus the field reflected by the metal plane $\Gamma\mathbf{h}_i$, plus the field scattered by the magnetic current above the layer. Reflection coefficient from a perfect electric plane is $\Gamma = 1$. Since the incident field cannot penetrate the perfectly conducting layer, the field below is only the one scattered by the magnetic current below:

$$\begin{aligned} \mathbf{h}^+ &= \mathbf{h}^- \\ \mathbf{h}_i(1 + \Gamma) + \mathbf{h}_{\text{scatt}}^+ &= \mathbf{h}_{\text{scatt}}^- \\ 2\mathbf{h}_i + \mathbf{h}_{\text{scatt}}\{\mathbf{m}_0\} &= \mathbf{h}_{\text{scatt}}\{-\mathbf{m}_0\} \end{aligned} \quad (7)$$

Writing the scattered field as convolution between the Green's function and the current gives

$$2\mathbf{m}_0(\boldsymbol{\rho}) * \mathbf{g}_{\text{PEC}}(\boldsymbol{\rho}) = -2\mathbf{h}_i \quad (8)$$

where $\boldsymbol{\rho} \equiv (x, y)$ and \mathbf{g}_{PEC} is the spatial dyadic Green's function giving the magnetic field radiated by an elementary magnetic source in the presence of the perfect electric conductor (PEC) plane. Finally, using the image theorem, a magnetic current located on an infinite metal plane can be replaced by twice the same current radiating in free space:

$$4\mathbf{m}_0(\boldsymbol{\rho}) * \mathbf{g}_{\text{fs}}(\boldsymbol{\rho}) = -2\mathbf{h}_i \quad (9)$$

where \mathbf{g}_{fs} is now the free space Green's function. Equation (9) represents the magnetic field integral equation to be solved, where the unknown is the magnetic current distribution \mathbf{m}_0 .

Expansion of the Unknown Current

To solve for the unknown magnetic current, we can expand it in a sum of 4 known basis functions \mathbf{f}_p , weighted by unknown coefficients \mathbf{v}_p , two for the x -oriented slot and 2 for the y -oriented one:

$$\mathbf{m}_0(\boldsymbol{\rho}) = \sum_{p=1}^4 v_p \mathbf{f}_p(\boldsymbol{\rho}) = [v_1 f_1(\boldsymbol{\rho}) + v_3 f_3(\boldsymbol{\rho})] \hat{\mathbf{x}} + [v_2 f_2(\boldsymbol{\rho}) + v_4 f_4(\boldsymbol{\rho})] \hat{\mathbf{y}}. \quad (10)$$

The step of expansion of the current in basis functions is typical of the Method of Moments, which is a widespread numerical method to solve Maxwell's equations. The 4 basis functions considered here are “*entire domain*”, i.e. defined over the entire unit cell. The choice of these basis functions derives from some intuitive considerations on what the current could look like on the slots. For more general problems, for which such intuition is missing, “*small domain*” basis functions are typically defined over small sub-domains of the unit cell (this approach is for example used in general purpose commercial software). The entire domain basis functions selected here are of two types (Figure 10):

- *1st Type: linear phase*

$$f_1(\boldsymbol{\rho}) = e^{-jk_{x0}x} m_t(y), \quad f_2(\boldsymbol{\rho}) = e^{-jk_{y0}y} m_t(x). \quad (11)$$

These two basis functions are characterized by constant amplitude and linear phase progression longitudinally, to account for the phase variation of the plane wave due to oblique incidence, while the transverse distribution is uniform:

$$m_t(y) = \frac{1}{w} \text{rect}\left[-\frac{w}{2}, \frac{w}{2}\right](y), \quad m_t(x) = \frac{1}{w} \text{rect}\left[-\frac{w}{2}, \frac{w}{2}\right](x). \quad (12)$$

The transverse distribution is chosen uniform and not edge-singular because it is easier to solve the problem analytically later, i.e. it is a convenience choice. The real distribution on metal strips or slots actually peaks at the edges, to satisfy the field singularity at metal edges. The Fourier transform of the functions in (11) are known and given by

$$F_1(k_{xm}, k_{ym}) = d_x \delta(m_x) \text{sinc}(k_{ym}w/2), \quad F_2(k_{xm}, k_{ym}) = d_y \delta(m_y) \text{sinc}(k_{xm}w/2). \quad (13)$$

where $\delta(\cdot)$ is the Kronecker delta.

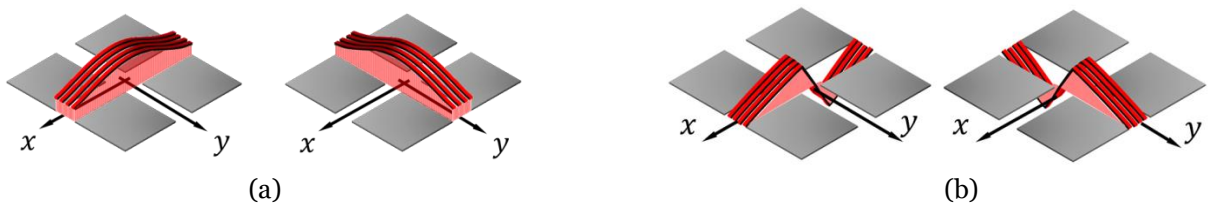


Figure 10. (a) First and (b) second type of basis functions. For the first type, the amplitude is constant and the phase varies linearly on the slot, thus the real and imaginary parts of the distribution are sinusoidal. Thus, the drawing in (a) is meant to represent the real or imaginary part of the distribution.

- *2nd Type: doublet function*

The first type of basis function does not account for the presence of the junction with the orthogonal slot. In other words this basis function would be the same if instead of patches (orthogonal slots along x and y), we were studying strips (slots only in one direction). To account for the effects of the junction, two additional basis functions are considered:

$$f_3(\boldsymbol{\rho}) = b_d(x) m_t(y), \quad f_4(\boldsymbol{\rho}) = b_d(x) m_t(x). \quad (14)$$

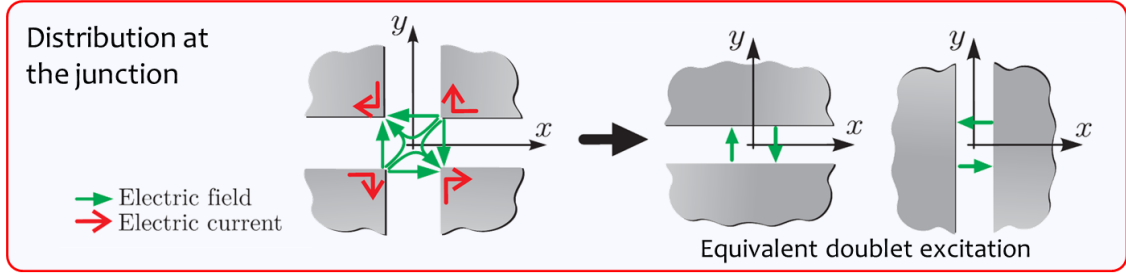
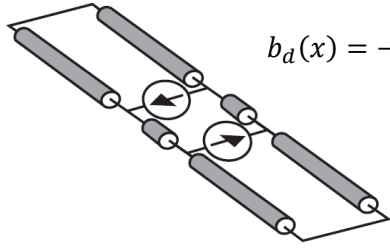


Figure 11. Electric field and current distribution at the junction.

These are anti-symmetric (odd) functions to describe the field distribution at the junction. Note that the current is 0 at the edges and at the center of the unit cell and is an odd function. At the intersection between the two slots, the field tends to distribute itself as shown in Figure 11, since both the current and the field have to satisfy the Kirchhoff law (sum of the current entering the junction is 0 and voltage across the contour of the junction is 0). The electric field distribution is compatible with two equivalent doublet excitations (anti-symmetric sources) that excite the slots and generate a current distribution as in Figure 10(b). To find a mathematical expression of the function $b_d(\cdot)$ we solve an equivalent transmission line problem with a doublet source excitation and shorted at the edges (to give 0 at the edges of the unit cell). The solution is



$$b_d(x) = -(e^{jk_0x} + \Gamma e^{-jk_0x})\text{rect}\left[-\frac{d_x}{2}, -\frac{w}{2}\right](x) + (e^{-jk_0x} + \Gamma e^{jk_0x})\text{rect}\left[\frac{w}{2}, \frac{d_x}{2}\right](x) + C x \text{rect}\left[-\frac{w}{2}, \frac{w}{2}\right](x)$$

$$\Gamma = -e^{-jk_0d_x} \quad C = 2/w \left(e^{-jk_0\frac{w}{2}} + \Gamma e^{jk_0\frac{w}{2}} \right) \quad (15)$$

The Fourier transform of (15) is known in closed form and reported in [7].

Galerkin Projection

Once the current expansion (10) is substituted in the integral equation, (9) becomes

$$\sum_{p=1}^4 v_p \mathbf{f}_p(\boldsymbol{\rho}) * \mathbf{g}(\boldsymbol{\rho}) = -2\mathbf{h}_i \quad (16)$$

where we used the notation $\mathbf{g} \triangleq 4\mathbf{g}_{fs}$ and the unknown coefficients of the method of moments are found by means of a projection operation onto some testing functions:

$$\langle \mathbf{f}_1(\boldsymbol{\rho}), \mathbf{f}_2(\boldsymbol{\rho}) \rangle = \int_{-\infty}^{\infty} \int_{-\infty}^{\infty} \mathbf{f}_1(\boldsymbol{\rho}) \cdot \mathbf{f}_2^*(\boldsymbol{\rho}) d\boldsymbol{\rho}. \quad (17)$$

If the testing functions are chosen to be the same as the basis function, which is done here, the testing method is referred to as Galerkin projection. Projecting both left hand side and right hand side onto $\mathbf{f}_q(\boldsymbol{\rho})$ with $q \in [1,2,3,4]$, we obtain four equation

$$\sum_{p=1}^4 -\langle \mathbf{f}_p(\boldsymbol{\rho}) * \mathbf{g}(\boldsymbol{\rho}), \mathbf{f}_q(\boldsymbol{\rho}) \rangle v_p = \langle 2\mathbf{h}_i(\boldsymbol{\rho}), \mathbf{f}_q(\boldsymbol{\rho}) \rangle, \quad \text{for } q = 1,2,3,4 \quad (18)$$

We define the mutual admittance $Y_{pq} = -\langle \mathbf{f}_p(\boldsymbol{\rho}) * \mathbf{g}(\boldsymbol{\rho}), \mathbf{f}_q(\boldsymbol{\rho}) \rangle$ and the forcing term (or known terms) currents as $i_q = \langle 2\mathbf{h}_i(\boldsymbol{\rho}), \mathbf{f}_q(\boldsymbol{\rho}) \rangle$. Hence, the four equations in (18) can written explicitly as

$$\begin{aligned}
v_1 Y_{11} + v_2 Y_{12} + v_3 Y_{13} + v_4 Y_{14} &= i_1 \\
v_1 Y_{21} + v_2 Y_{22} + v_3 Y_{23} + v_4 Y_{24} &= i_2 \\
v_1 Y_{31} + v_2 Y_{32} + v_3 Y_{33} + v_4 Y_{34} &= i_3 \\
v_1 Y_{41} + v_2 Y_{42} + v_3 Y_{43} + v_4 Y_{44} &= i_4
\end{aligned} \tag{19}$$

or, with a matrix notation, as

$$\begin{bmatrix} Y_{11} & Y_{12} & Y_{13} & Y_{14} \\ Y_{21} & Y_{22} & Y_{23} & Y_{24} \\ Y_{31} & Y_{32} & Y_{33} & Y_{34} \\ Y_{41} & Y_{42} & Y_{43} & Y_{44} \end{bmatrix} \cdot \begin{bmatrix} v_1 \\ v_2 \\ v_3 \\ v_4 \end{bmatrix} = \begin{bmatrix} i_1 \\ i_2 \\ i_3 \\ i_4 \end{bmatrix} \quad \text{or in compact form } \mathbf{Y} \cdot \mathbf{v} = \mathbf{i} \tag{20}$$

Equation (20) could be solved easily to find the unknowns by simply inverting the relation as $\mathbf{v} = \mathbf{Y}^{-1} \cdot \mathbf{i}$. However this solution, although accurate and computationally efficient, would still be numerical and would not give any physical insight. Therefore, we make in the following section an effort to derive a more explicit solution that lends itself to an equivalent circuit representation and to some physical interpretation.

Admittance Matrix Simplifications

All the terms of the admittance matrix and the current vector can be written in closed form, the generic expression of the mutual admittance is

$$Y_{qp} = -\langle \mathbf{f}_p(\boldsymbol{\rho}) * \mathbf{g}(\boldsymbol{\rho}), \mathbf{f}_q(\boldsymbol{\rho}) \rangle = - \int_{-\infty}^{\infty} \int_{-\infty}^{\infty} \int_{-\infty}^{\infty} \int_{-\infty}^{\infty} \mathbf{f}_p(\boldsymbol{\rho}) \mathbf{g}(\boldsymbol{\rho} - \boldsymbol{\rho}') \cdot \mathbf{f}_q^*(\boldsymbol{\rho}) d\boldsymbol{\rho} d\boldsymbol{\rho}'. \tag{21}$$

where two integrals come from the convolution and two from the projection. It is convenient to evaluate (21) in the spectral domain, since we know the Green's function of stratified media and also, due to periodicity, we can apply the Floquet Theorem. In the spectral domain, the convolution becomes a product and, as a consequence of the Floquet theorem, the spectrum is discrete and integrals become sums:

$$Y_{qp} = -\frac{1}{d_x} \frac{1}{d_y} \sum_{m_x=-\infty}^{\infty} \sum_{m_y=-\infty}^{\infty} \mathbf{F}_p(k_{xm}, k_{ym}) \mathbf{G}(k_{xm}, k_{ym}) \cdot \mathbf{F}_q^*(-k_{xm}, -k_{ym}). \tag{22}$$

When evaluating all Y_{qp} and i_q , it can be shown that some of the terms are close to 0 and can be neglected. These represent the projection of a plane wave onto the odd function (can be neglected since the negative and positive contributions cancel out). Thus $Y_{24} \approx Y_{13} \approx 0$ and $i_3 \approx i_4 \approx 0$, so that (20) can be written as

$$\begin{bmatrix} Y_{11} & Y_{12} & 0 & Y_{14} \\ Y_{21} & Y_{22} & Y_{23} & 0 \\ 0 & Y_{32} & Y_{33} & Y_{34} \\ Y_{41} & 0 & Y_{43} & Y_{44} \end{bmatrix} \cdot \begin{bmatrix} v_1 \\ v_2 \\ v_3 \\ v_4 \end{bmatrix} = \begin{bmatrix} i_1 \\ i_2 \\ 0 \\ 0 \end{bmatrix}. \tag{23}$$

If one is interested only in the weights v_1 and v_2 , after some algebraic steps, the reduced 2×2 matrix becomes

$$\begin{bmatrix} Y_{11} - \frac{Y_{41}Y_{14}Y_{33}}{Y_{33}Y_{44} - Y_{34}Y_{43}} & Y_{12} + \frac{Y_{32}Y_{43}Y_{14}}{Y_{33}Y_{44} - Y_{34}Y_{43}} \\ Y_{21} + \frac{Y_{41}Y_{23}Y_{34}}{Y_{33}Y_{44} - Y_{34}Y_{43}} & Y_{22} - \frac{Y_{32}Y_{23}Y_{44}}{Y_{33}Y_{44} - Y_{34}Y_{43}} \end{bmatrix} \cdot \begin{bmatrix} v_1 \\ v_2 \end{bmatrix} = \begin{bmatrix} i_1 \\ i_2 \end{bmatrix} \quad \text{or} \quad \mathbf{Y}_{\text{red}} \cdot \begin{bmatrix} v_1 \\ v_2 \end{bmatrix} = \begin{bmatrix} i_1 \\ i_2 \end{bmatrix}. \quad (24)$$

(24) refers to current oriented along x and y . To link the currents directly to the TE and TM components, it is convenient to project the current from the x,y to the TE,TM components. This can be done by means of the following rotation matrix:

$$\mathbf{R} = \begin{bmatrix} \cos \phi & \sin \phi \\ -\sin \phi & \cos \phi \end{bmatrix}. \quad (25)$$

Pre-multiplying left and right by \mathbf{R} and using $\mathbf{R}^T \mathbf{R} = \mathbf{I}$ (identity matrix), one obtains

$$\mathbf{R} \mathbf{Y}_{\text{red}} \mathbf{R}^T \begin{bmatrix} v_1 \\ v_2 \end{bmatrix} = \mathbf{R} \begin{bmatrix} i_1 \\ i_2 \end{bmatrix} \quad \text{or} \quad \mathbf{Y}_{\text{TETM}} \begin{bmatrix} v_{\text{TE}} \\ v_{\text{TM}} \end{bmatrix} = \begin{bmatrix} i_{\text{TE}} \\ i_{\text{TM}} \end{bmatrix}. \quad (26)$$

with $\mathbf{Y}_{\text{TETM}} = \mathbf{R} \mathbf{Y}_{\text{red}} \mathbf{R}^T$, $\begin{bmatrix} v_{\text{TE}} \\ v_{\text{TM}} \end{bmatrix} = \mathbf{R} \begin{bmatrix} v_1 \\ v_2 \end{bmatrix}$ and $\begin{bmatrix} i_{\text{TE}} \\ i_{\text{TM}} \end{bmatrix} = \mathbf{R} \begin{bmatrix} i_1 \\ i_2 \end{bmatrix}$.

Equivalent Circuit of Single Layer

The described algebraic steps, although tedious, enables representation of the admittance matrix with an equivalent circuit that gives physical insight. When writing explicitly the expression of \mathbf{Y}_{TETM} , one obtains

$$\mathbf{Y}_{\text{TETM}} = \mathbf{Y}_{\text{TL}} + \mathbf{Y}_{\text{ADL}} = \begin{bmatrix} 2/Z_{0\text{TE}} & 0 \\ 0 & 2/Z_{0\text{TM}} \end{bmatrix} + \begin{bmatrix} jB \left(1 - \frac{\sin^2 \theta}{2}\right) & 0 \\ 0 & jB \end{bmatrix}. \quad (27)$$

This simplified expression allows for some discussion on the physical behavior of the single layer of patches:

- The matrix in (27) is diagonal: this means that the TE and TM modes are uncoupled, at least for subwavelength patches. In other words, under TE plane-wave incidence, the layer can only scatter TE waves, and under TM incidence it can only scattered TM waves. This property was previously observed in literature, but now it is also proven mathematically with a rigorous solution.
- The matrix in (27) does not depend on ϕ , for patches small compared to the wavelength. The scattering behaviour of the layer is not dependent on the azimuthal angle of incidence. This characteristic is not intuitive since for diagonal plane incidence the geometry is different compared to the main planes. This property was also known before, but now proven rigorously.
- The first part of the matrix, \mathbf{Y}_{TL} , can be represented as the parallel of two transmission lines, representing the propagation of the TE and TM plane waves in free space.
- The second part of the matrix, \mathbf{Y}_{ADL} , can be represented as a shunt impedance that describes the layer reactance. More specifically, B is the layer susceptance, given by

$$B \approx \frac{\omega \epsilon_0 d_y}{\pi} \sum_{m \neq 0} \frac{|\text{sinc}(\pi m w / d_y)|^2}{|m|}. \quad (28)$$

The complete equivalent circuit becomes the one in Figure 12. When a generic plane wave impinges on the layer, its TM and TE component can be describe with two equivalent decoupled transmission lines, where the layer is described as an equivalent shunt impedance, which is a

closed-form expression depending on the geometrical parameters of the layer. As a validation of the formula in (28), Figure 13 shows an example of layer impedance calculation, comparing the analytical method described here with HFSS.

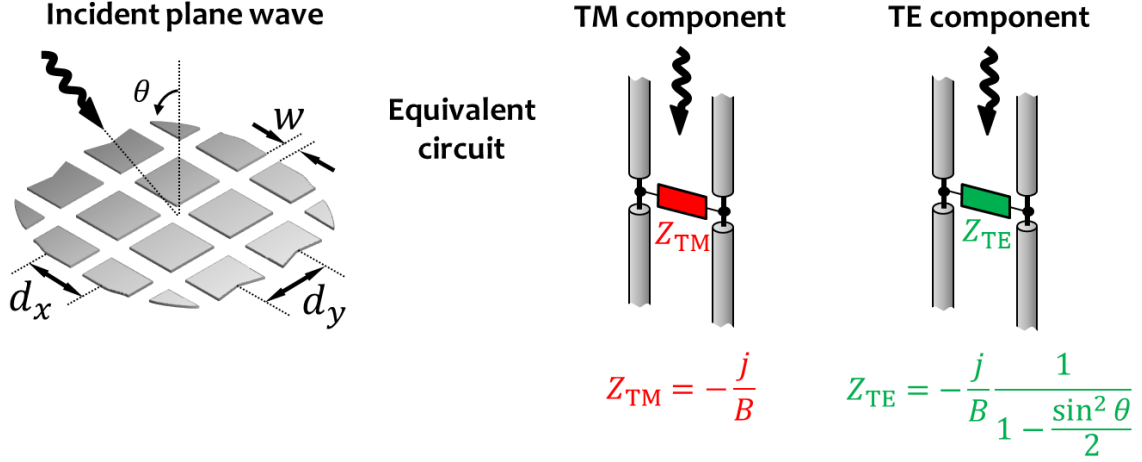


Figure 12. Equivalent circuit of single layer of patches under generic plane-wave incidence.

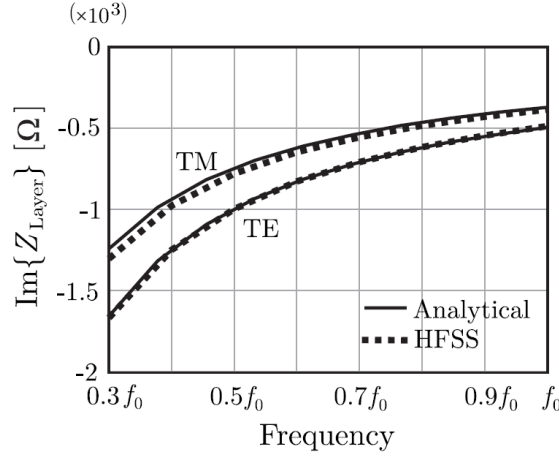


Figure 13. Example of comparison between this method and HFSS commercial software, for the calculation of the equivalent layer impedance.

The closed-form expression in (28) is not the only existing formula that can be found in literature to describe a layer of electrically small patches. Other equivalent expressions are given, for example, in [8]-[11]. The main advantage of the formula given here with respect to earlier works is that, unlike the other methods, the one given here is easy to generalize to multiple layers.

2.2 Multiple Layers

Infinite Stack of Layers

To extend the method to multiple layers, we first consider an infinite stack of identical layers. Such a stack is shown in Figure 14(a), where each layer is numbered with the index n_z . Taking the two regions above and below $n_z = 0$ and applying the equivalence theorem as shown in Figure 14(b) yields two cavities surrounded by PEC, with three unknown magnetic currents \mathbf{m}_{-1} , \mathbf{m}_0 , and \mathbf{m}_1 , located in the regions corresponding to the gaps in the original problem.

The magnetic currents \mathbf{m}_{n_z} are related to the incident electric field \mathbf{e}_i through

$$\mathbf{m}_{n_z} = \mathbf{e}_i(\boldsymbol{\rho}, z = n_z d_z) \times \hat{\mathbf{z}} \quad (29)$$

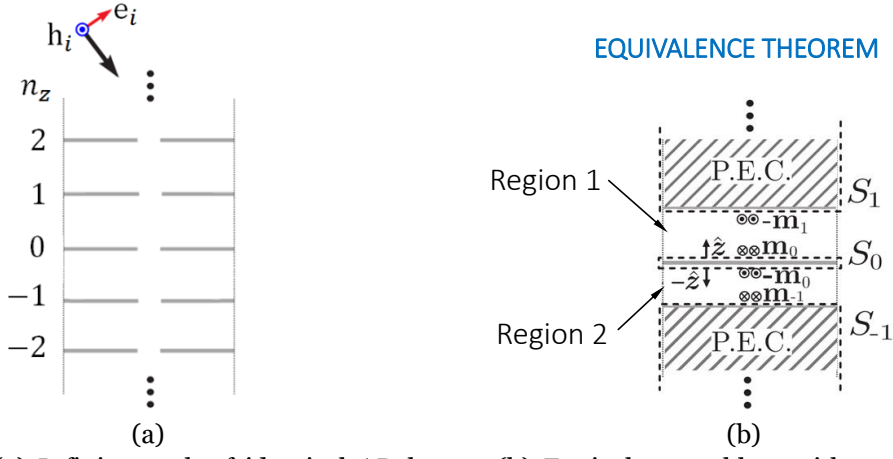


Figure 14. (a) Infinite stack of identical AD layers. (b) Equivalent problem with two regions around the central layer at $n_z = 0$.

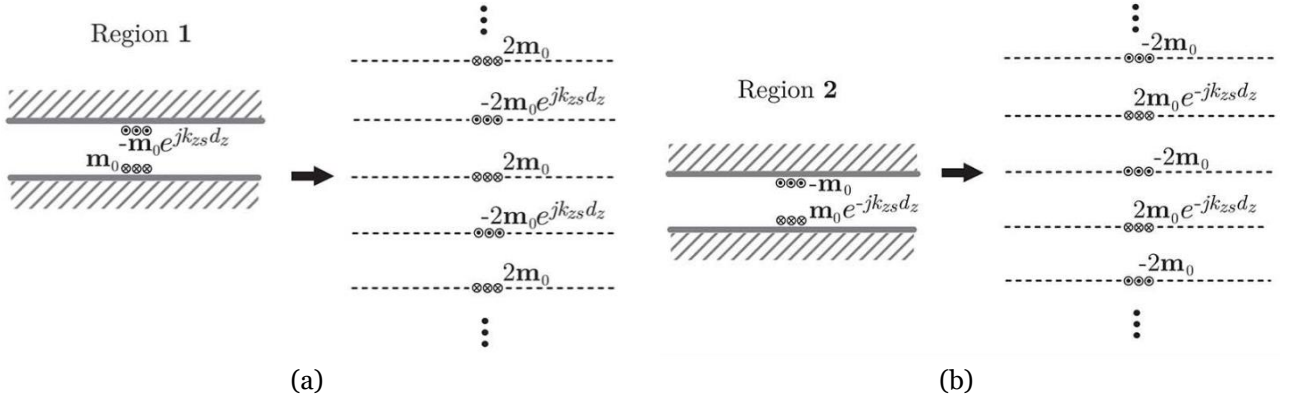


Figure 15. Situation after application of the image theorem in the regions (a) above and (b) below the layer at $n_z = 0$.

Due to the periodicity of the structure along z , we can relate the current on the different layers as

$$\mathbf{m}_{\pm 1}(\boldsymbol{\rho}) = \mathbf{m}_0(\boldsymbol{\rho})e^{\pm jk_{zs}d_z} \quad (30)$$

where the phase term accounts for the phase of the wave travelling through the stratification, with an unknown wavenumber k_{zs} . Applying the image theorem yields two situations for the two regions, which are shown in Figure 15. The integral equation is found by again imposing the continuity of the transverse magnetic field at $z = 0$ ($\mathbf{h}^+ = \mathbf{h}^-$). The magnetic field in region 1, \mathbf{h}^+ , because of the image theorem, can be expressed as the field scattered by an infinite number of sources as in Figure 15(a). Analogously, the magnetic field in region 2, \mathbf{h}^- , can be calculated as the sum of infinite contributions and in Figure 15(b). Thus imposing $\mathbf{h}^+ - \mathbf{h}^- = 0$ gives

$$\begin{aligned} \sum_{n_z, \text{even}} \int_{-\infty}^{\infty} \int_{-\infty}^{\infty} 4\mathbf{m}_0(\boldsymbol{\rho}') \mathbf{g}(\boldsymbol{\rho} - \boldsymbol{\rho}', n_z d_z, z = 0) d\boldsymbol{\rho}' \\ - \sum_{n_z, \text{odd}} \int_{-\infty}^{\infty} \int_{-\infty}^{\infty} 2(e^{jk_{zs}d_z} + e^{-jk_{zs}d_z}) \mathbf{m}_0(\boldsymbol{\rho}') \mathbf{g}(\boldsymbol{\rho} - \boldsymbol{\rho}', n_z d_z, z = 0) d\boldsymbol{\rho}' = 0 \end{aligned} \quad (31)$$

Note that \mathbf{h}_i does not appear in (31) since the incident field cannot penetrate the top PEC. We use now the approximation of small argument of the cosine:

$$2(e^{jk_{zs}d_z} + e^{-jk_{zs}d_z}) = 4 \cos(k_{zs}d_z) \approx 4 \quad (32)$$

which is valid for $k_z d_z \ll 1$. This is true when the distance between layers is small compared to the wavelength, which is the case for ADLs. Therefore (31) can be simplified as

$$\sum_{n_z, \text{even}} \int_{-\infty}^{\infty} \int_{-\infty}^{\infty} 4\mathbf{m}_0(\boldsymbol{\rho}') \mathbf{g}(\boldsymbol{\rho} - \boldsymbol{\rho}', n_z d_z, z = 0) d\boldsymbol{\rho}' - \sum_{n_z, \text{odd}} \int_{-\infty}^{\infty} \int_{-\infty}^{\infty} 4\mathbf{m}_0(\boldsymbol{\rho}') \mathbf{g}(\boldsymbol{\rho} - \boldsymbol{\rho}', n_z d_z, z = 0) d\boldsymbol{\rho}' \approx 0 \quad (33a)$$

or

$$\sum_{n_z} (-1)^{n_z} \int_{-\infty}^{\infty} \int_{-\infty}^{\infty} 4\mathbf{m}_0(\boldsymbol{\rho}') \mathbf{g}(\boldsymbol{\rho} - \boldsymbol{\rho}', n_z d_z, z = 0) d\boldsymbol{\rho}' \approx 0 \quad (33b)$$

We can solve this integral equation using the same method as the one used for the single layer case, where the unknown magnetic current is expanded into entire domain basis functions, applying Galerkin projection and reducing the resulting matrix into TE and TM components. The only difference compared to the single layer is modifying the higher order Floquet modes of the Green's function to account for the infinite sum on the indices n_z arising from (33b). We use the identity

$$\sum_{n_z=-\infty}^{\infty} (-1)^{n_z} e^{-jk_z |n_z| d_z} = j \tan \frac{k_z d_z}{2} \quad (34)$$

to find the layer susceptance of the infinite cascade as the same expression of the reactance of the single layer in (28), where each term is multiplied by the tangent term, which accounts for the inter-layer reactive coupling:

$$B_{\infty} \approx \frac{\omega \varepsilon_0 d_y}{\pi} \sum_{m \neq 0} \frac{\left| \text{sinc} \left(\frac{\pi m w}{d_y} \right) \right|^2}{|m|} \times j \tan \left(\frac{-j \pi |m| d_z}{d_y} \right). \quad (35)$$

Equivalent Circuit of an Infinite Stack of Layers

The equivalent circuit of multiple layers shown in Figure 16 is an extension of the equivalent circuit derived for the single layer case. The TM and TE components are again described with two equivalent decoupled transmission lines, with layers described as equivalent shunt impedances, which are a closed-form expression depending on the geometrical parameters of the layers.

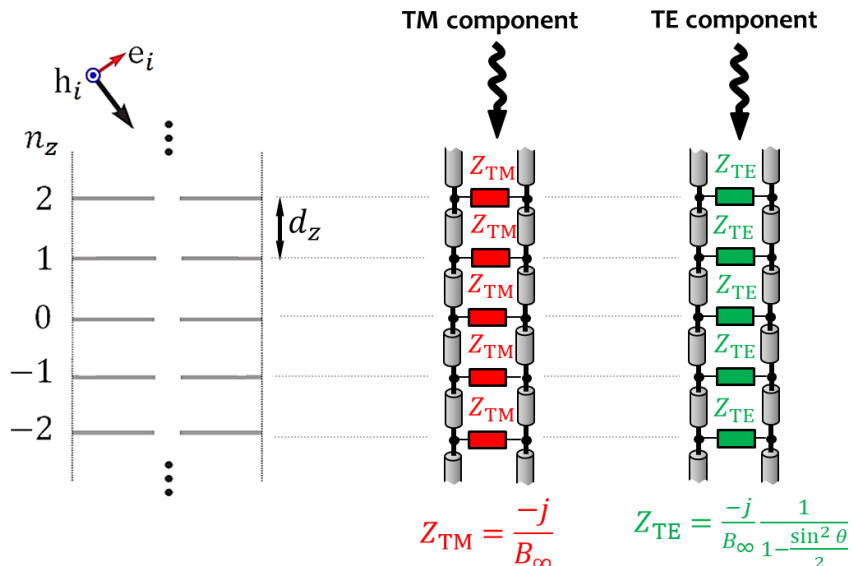


Figure 16. Equivalent circuit for an infinite number of layers.

Finite Number of Layers

When a finite number of layers is considered, with indexes $n_z = 1, \dots, N_z$, the reactance of the inner layers ($n_z = 2, \dots, N_z - 1$) can be still approximated using the infinite cascade solution. This is because the equivalent reactance of a layer is dominated by the coupling with the two layers immediately above and below. However, the first and last layer of the finite cascade ($n_z = 1, n_z = N_z$) are not well described by the infinite cascade solution, since they couple with other layers only at one side. To account for this truncation effect, a semi-infinite cascade problem can also be solved (see Figure 17). For this we use the same procedure as the infinite case, and the identity

$$\sum_{n_z=-\infty}^0 (-1)^{n_z} e^{jk_z n_z d_z} = \sum_{n_z=0}^{\infty} (-1)^{n_z} e^{-jk_z n_z d_z} = \frac{1}{2} + \frac{j}{2} \tan \frac{k_z d_z}{2}. \quad (36)$$

Thus, the susceptance of the outer layers in the finite artificial dielectric stack becomes

$$B_{\text{semi-}\infty} \approx \frac{\omega \varepsilon_0 d_y}{\pi} \sum_{m \neq 0} \frac{\left| \text{sinc} \left(\frac{\pi m w}{d_y} \right) \right|^2}{|m|} \times \left(\frac{1}{2} + \frac{j}{2} \tan \left(\frac{-j\pi |m| d_z}{d_y} \right) \right). \quad (37)$$

Figure 18 shows the scattering parameters for normal incidence of a cascade of 4 layers, compared to the commercial solver HFSS. Two cases are considered: (1) all layers approximated with the infinite cascade solution and (2) infinite cascade solution for inner layers, while semi-infinite solution for top and bottom layers. It is apparent that including the semi-infinite solution for the edge layers improves the accuracy of the model and approximates better the truncation effects due to the finite number of layers.

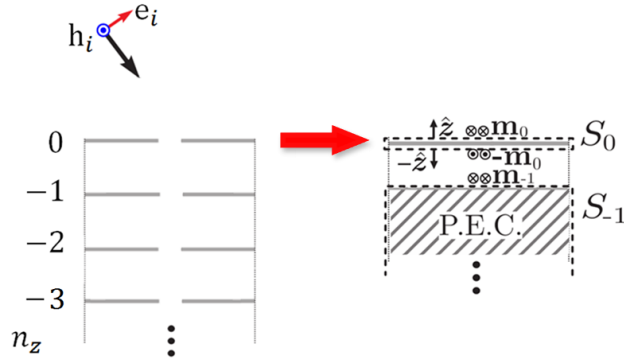


Figure 17. (a) Semi-infinite stack of identical layers and (b) equivalent problem.

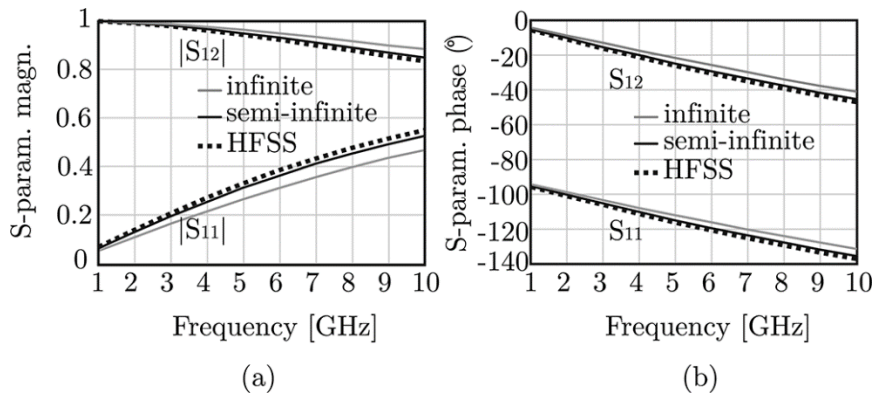


Figure 18. (a) Magnitude and (b) phase of the scattering parameters incident normal to a cascade of 4 layers.

Equivalent Circuit of a Finite Number of Layers

The equivalent circuit of the finite cascade (Figure 19) is very similar to the infinite-layer case, except that there is now a finite number of impedances. In addition to this, the outer layers are represented using the semi- ∞ solution. The values of the impedances are

$$Z_{\text{semi-}\infty, \text{TM}} = -\frac{j}{B_{\text{semi-}\infty}} \quad Z_{\text{semi-}\infty, \text{TE}} = -\frac{j}{B_{\text{semi-}\infty}} \frac{1}{1 - \frac{\sin^2 \theta}{2}} \quad (38)$$

$$Z_{\infty, \text{TM}} = -\frac{j}{B_{\infty}} \quad Z_{\infty, \text{TE}} = -\frac{j}{B_{\infty}} \frac{1}{1 - \frac{\sin^2 \theta}{2}} \quad (39)$$

where θ is the angle of incidence and B_{∞} and $B_{\text{semi-}\infty}$ are given in (35) and (37), respectively.

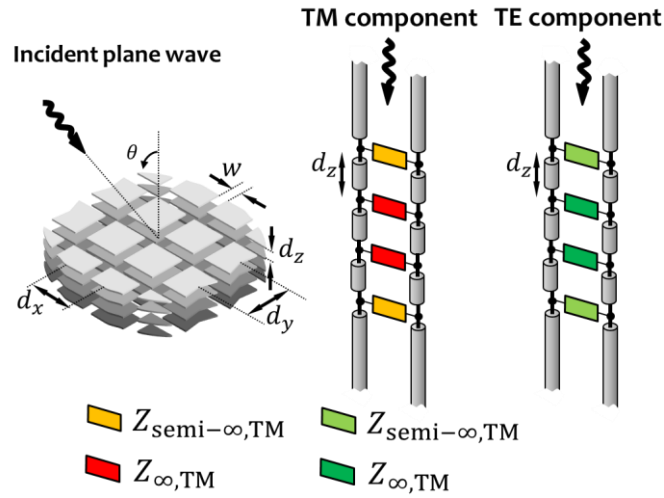


Figure 19. Equivalent circuit of a finite artificial dielectric stratification.

2.3 Shifted Layers

In the analysis so far, all the layers in the artificial dielectric stack have been horizontally aligned. However, the lateral displacement of the layers is an important parameter in the design of the ADL material. More specifically, much higher equivalent refractive indexes can be realized by alternatively shifting the layers, compared to the aligned case. This is due to an increased delay experienced by the field travelling through the ADLs, as highlighted in Figure 20(a) and (b), and also to a stronger capacitance between layers, when shift is applied. The refractive index is shown in Figure 20(c) to be much higher when shifted layers are used. Therefore, the range of equivalent permittivities that can be realized with a certain manufacturing technology is greatly extended when shifts between layers is applied. Moreover the shift allows for more flexible ADL designs: e.g., a given ADL slab with aligned layers can be equivalently realized with a reduced number of layers when shift is applied; or, if one wants to design an ADL with height equal to a quarter of the effective wavelength, the overall thickness can be reduced when shifting the layers.

Since the shift is a key parameter in the ADL design, the analysis for the aligned case is extended to also obtain a solution for the non-aligned case in [14]. The geometry definition is presented in Figure 21. The procedure used for the infinite aligned case is used here, except that the odd sum in (31) can no longer be directly expressed in terms of \mathbf{m}_0 due to the spatial displacement of the alternately shifted layers. As such, the current is expressed in terms of the current \mathbf{m}_{-1} to find the integral equation

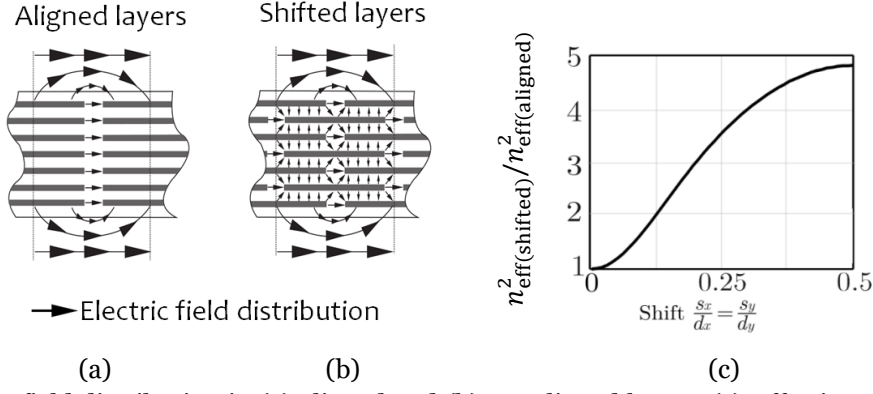


Figure 20. Electric field distribution in (a) aligned and (b) nonaligned layers. (c) Effective refractive index as a function of shift.

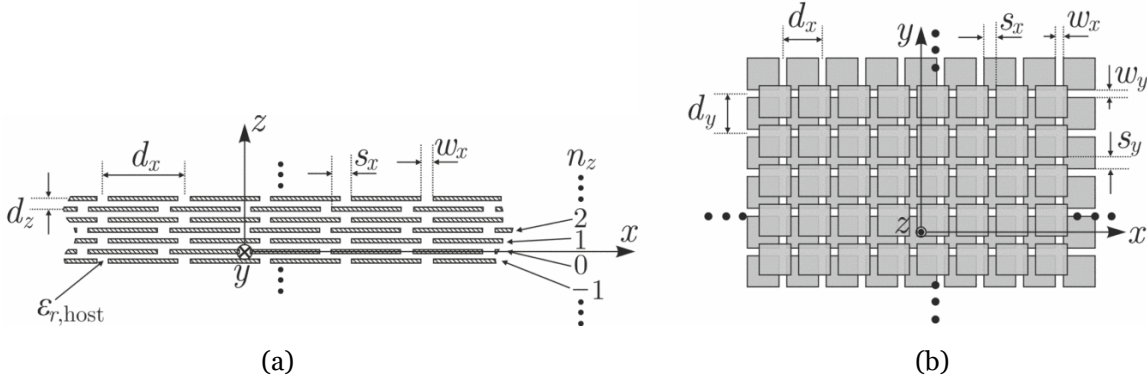


Figure 21. Illustration of the geometrical parameters of the shifted ADLs. (a) Side and (b) top view.

$$\begin{aligned}
 & \sum_{n_z, \text{even}} \int_{-\infty}^{\infty} \int_{-\infty}^{\infty} 4\mathbf{m}_0(\boldsymbol{\rho}') \mathbf{g}(\boldsymbol{\rho} - \boldsymbol{\rho}', n_z d_z, z=0) d\boldsymbol{\rho}' \\
 & - \sum_{n_z, \text{odd}} \int_{-\infty}^{\infty} \int_{-\infty}^{\infty} 2(e^{jk_{zs}2d_z} + 1) \mathbf{m}_{-1}(\boldsymbol{\rho}') \mathbf{g}(\boldsymbol{\rho} - \boldsymbol{\rho}', n_z d_z, z=0) d\boldsymbol{\rho}' = 0.
 \end{aligned} \quad (40)$$

The current \mathbf{m}_{-1} cannot be directly related to the current \mathbf{m}_0 using the standard Floquet boundary conditions. Instead, we have to use a condition referred to as “higher symmetry” (combination of mirroring and translation) [15]: in this the magnetic currents on the two layers can be assumed to be equal in amplitude and to differ only from a spatial displacement and a phase term. As such, it is expressed as

$$\mathbf{m}_{-1} = \mathbf{m}_0(\boldsymbol{\rho}' - \mathbf{s}) e^{-j\mathbf{k}_{\rho s} \cdot \mathbf{s}} e^{-jk_{zs}d_z}, \quad (41)$$

where $\mathbf{s} = s_z \hat{\mathbf{x}} + s_y \hat{\mathbf{y}}$ is the shift between the layers and $\mathbf{k}_{\rho s} = k_{xs} \hat{\mathbf{x}} + k_{ys} \hat{\mathbf{y}}$ is the unknown wave vector of the transverse wave propagating between the layers. Using (41) and fixing $s_x = s_y$ to retain the azimuth-independent properties of the ADL, the integral equation in (40) can be solved in the same way as for the aligned case. The layer susceptance is found to be

$$B_{\infty} \approx \frac{\omega \epsilon_0 d_y}{\pi} \sum_{m \neq 0} \frac{\left| \text{sinc}\left(\frac{\pi m w}{d_y}\right) \right|^2}{|m|} \times \left(-j \cot\left(\frac{-j2\pi|m|d_z}{d_y}\right) + j e^{j2\pi m \frac{s_y}{d_y}} \csc\left(\frac{-j2\pi|m|d_z}{d_y}\right) \right). \quad (42)$$

Similarly, the procedure used for the semi- ∞ aligned case is repeated to find the layer susceptance for the semi- ∞ case as

$$B_\infty \approx \frac{\omega \varepsilon_0 d_y}{\pi} \sum_{m \neq 0} \frac{\left| \text{sinc}\left(\frac{\pi m w}{d_y}\right) \right|^2}{|m|} \times \left(\frac{1}{2} - \frac{j}{2} \cot\left(\frac{-j2\pi|m|d_z}{d_y}\right) + \frac{j}{2} e^{j2\pi m \frac{s_y}{d_y}} \csc\left(-\frac{j2\pi|m|d_z}{d_y}\right) \right). \quad (43)$$

The susceptance in (42) and (43) combined with the expressions in (38) and (39) can be used in the equivalent circuit of the ADL with shifted layers. All formulas given in this documents have been validated with commercial solvers (CST or HFSS) and shown to be accurate for

- Generic plane wave incidence, i.e. for any angle of incidence, any polarization (TE or TM);
- Arbitrary small distance between layers, because higher order Floquet mode interaction between layers is accounted for;
- Any number or layers, from 1 to ∞ , since the truncation effects are taken into account.

The only important approximation, needed for the validity of the models, is related to the period of the ADL unit cell and the size of the patches, which must be small compared to the wavelength. Nevertheless, numerical results and comparison with full wave simulation show that the given formulas can be practically used with fair accuracy for unit cell spacing up to of $\lambda/4$.

3 Near Source Excitation

3.1 Radiation Patterns

The main advantage of having derived the spectral Green's function of ADLs is that we can now design antennas in the presence of ADLs with a fast semi-analytical simulation tool. In fact, the process of designing an antenna often involves an optimization phase during which the best geometrical parameters to achieve some target performance are selected. Such an optimization requires a very large number of simulations and becomes impractical or even impossible if a single simulation is computationally too demanding or the number of geometrical parameters is too large. In the specific example of ADLs, the theoretical models described in this document are fundamental to enable the design, that would not be possible otherwise.

Since we know the response of the ADL for any generic plane wave, we can expand the field radiated by any source located in close proximity of the ADL as spectrum of plane waves. For each plane wave we then apply the equivalent transmission line model derived in the previous sections. This approach allows, for example, to calculate the impedance or the radiation pattern of an antenna radiating in the presence of the ADL with a much faster simulation than a commercial electromagnetic solver (computing time of seconds as opposed to hours).

By the asymptotic evaluation of the radiation integral with the stationary phase point method, the far-field magnetic field radiated a magnetic current distribution $\mathbf{m}_s(x', y')$, defined on the plane $z' = 0$, can be expressed as

$$\mathbf{h}(\mathbf{r}) \approx j k_{z0} \mathbf{M}_s(k_{x0}, k_{y0}) \mathbf{G}_{\text{ADL}}(k_{x0}, k_{y0}, z) \frac{e^{-jkr}}{2\pi r}. \quad (42)$$

where \mathbf{M}_s is the Fourier transform of the source magnetic current \mathbf{m}_s , $\mathbf{r} \equiv (x, y, z) \equiv (r, \theta, \phi)$ is the observation point, and $k_{x0} = k_0 \sin \theta \cos \phi$, $k_{y0} = k_0 \sin \theta \sin \phi$, $k_{z0} = k_0 \cos \theta$. For example, the field radiated by a double slot with an ADL slabs [12] is shown in Figure 22.

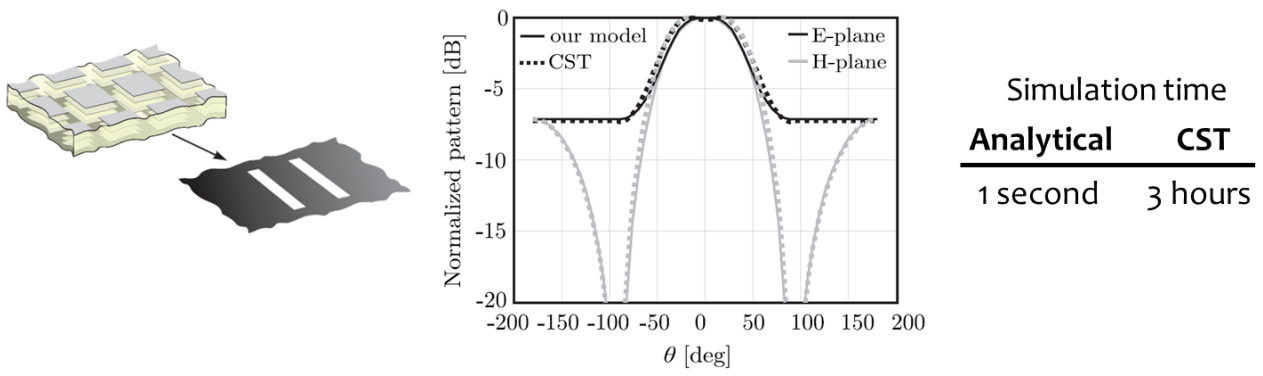


Figure 22. Example of far field radiated by a double slot with an ADL slabs, simulated with CST and with the spectral method presented here.

3.2 Dispersion Analysis

The availability of the spectral Green's function of the ADLs also gives the possibility to study the dominant contributions of the field propagating in the structure, for near source excitation. For example, in previous parts of this course it was described that the polar singularities of the spectral Green's function of a stratified medium can be associated with surface waves and leaky waves.

A similar exercise can be done for artificial dielectric grounded slab, by finding the poles of \mathbf{G}_{ADL} (solutions of the dispersion equation $1/\mathbf{G}_{\text{ADL}} = 0$). Figure 23 shows the poles of the spectral Green's function for an ADL grounded slab with 9 layers in free space, with effective permittivity of 10 for normal incidence and total height of $\lambda_{\text{eff}}/4$ at 10 GHz. Poles are shown in the complex plane and in a dispersion diagram, for both the TE and TM cases, as a function of the frequency. It can be seen that leaky wave poles exist for both TE and TM propagation, while surface waves only for TE propagation.

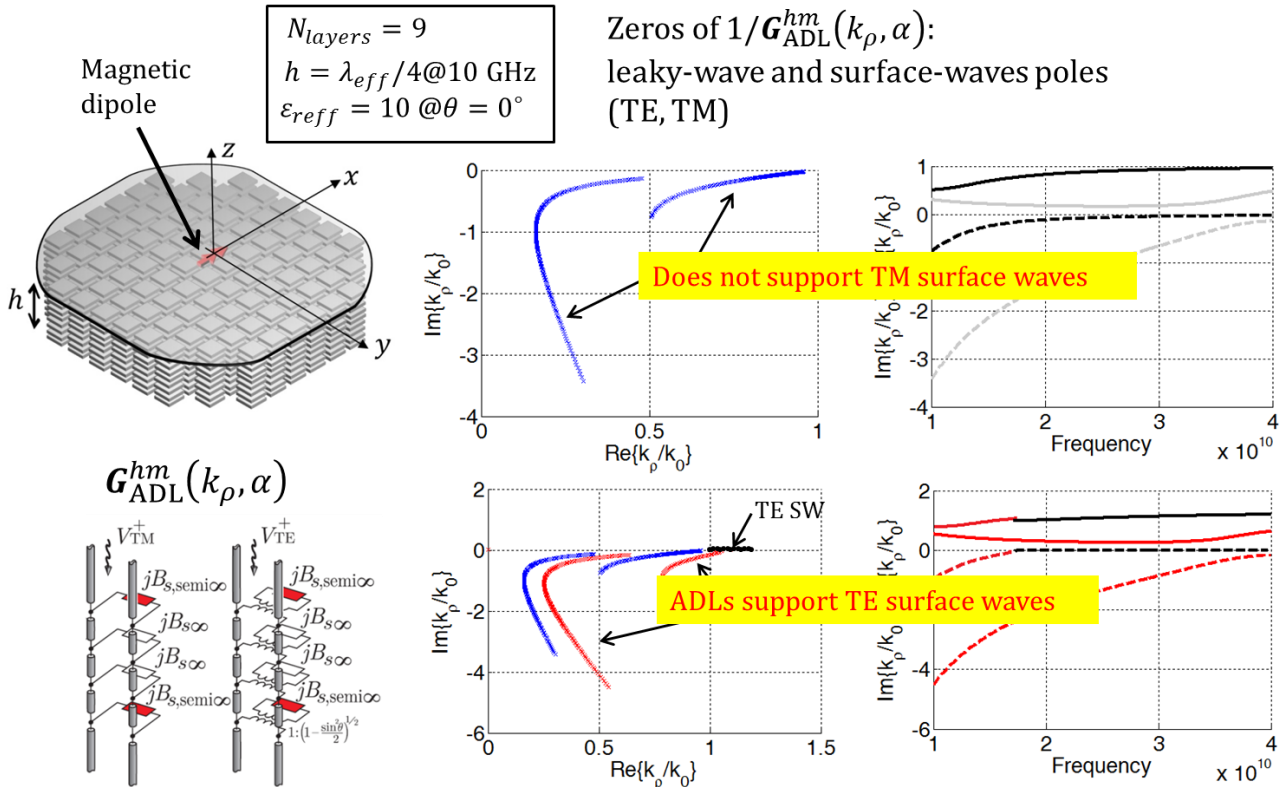


Figure 23. Polar singularity of the spectral Green's function for an ADL grounded slab.

This is because the ADL effective refractive index for angle of incidence of 90 degrees tends to 1 for the TM component, but not for TE. Nevertheless, TE surface waves appear at quite high frequency, for which the dielectric height is almost half of the effective wavelength. Thus, for realistic slabs designs (approx. quarter wavelength) the TE surface wave is below cut-off and does not cause surface wave losses.

4 Homogenization

4.1 Parameter Retrieval

To effectively design an artificial dielectric stratification, it is convenient to be able to assign to it equivalent homogeneous dielectric parameters. As such, it is desirable to determine the effective constitutive parameters, that is, the tensors $\bar{\epsilon}_{\text{eff}}$ and $\bar{\mu}_{\text{eff}}$. A technique to extract these from the reflection coefficients of a given stratification is presented in [17], and a simplified version of those equations is reported here for completeness.

The technique is based on extracting the unknown permittivity and permeability tensors of an anisotropic material from the knowledge of the S-parameters of a plane wave incidence from two angles, $\theta_i = 0$ and an arbitrary $\theta_i = \theta_1$, for TE and TM incidence, respectively.

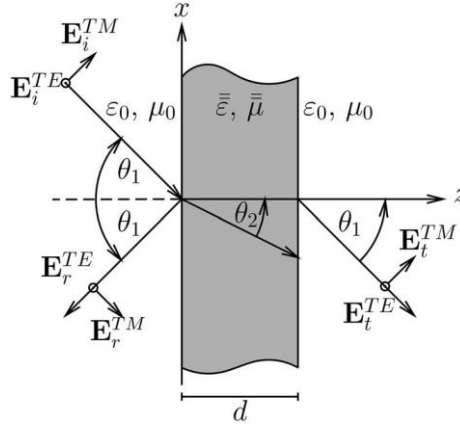


Figure 24. Illustration of the situation when extracting the effective constitutive parameters from an arbitrary given stratification.

In the case of the ADLs, the transmission line model described in Chapter 2 is used to determine the reflection coefficients of the stratification when it is illuminated in free space by a plane wave indented at these angles. The reflection coefficients S^{TE} and S^{TM} are obtained for TE and TM incidence, respectively. From this, the permittivity and permeability tensors are obtained as

$$\bar{\epsilon} = \epsilon_0 \begin{pmatrix} \epsilon_x & 0 & 0 \\ 0 & \epsilon_y & 0 \\ 0 & 0 & \epsilon_z \end{pmatrix} \quad \bar{\mu} = \mu_0 \begin{pmatrix} \mu_x & 0 & 0 \\ 0 & \mu_y & 0 \\ 0 & 0 & \mu_z \end{pmatrix}, \quad (44)$$

where the diagonal elements are found as

$$\begin{aligned} \epsilon_x &= \frac{n_{\theta_i=0}^{\text{TM}}}{\eta_{\theta_i=0}^{\text{TM}}} & \epsilon_y &= \frac{n_{\theta_i=0}^{\text{TE}}}{\eta_{\theta_i=0}^{\text{TE}}} & \epsilon_z &= \frac{\epsilon_x \sin^2 \theta_i}{\sin^2 \theta_1 - (n^{\text{TM}})^2 + (n_{\theta_i=0}^{\text{TM}})^2} \\ \mu_x &= n_{\theta_i=0}^{\text{TE}} \eta_{\theta_i=0}^{\text{TE}} & \mu_y &= n_{\theta_i=0}^{\text{TM}} \eta_{\theta_i=0}^{\text{TM}} & \mu_z &= \frac{\mu_x \sin^2 \theta_i}{\sin^2 \theta_1 - (n^{\text{TE}})^2 + (n_{\theta_i=0}^{\text{TE}})^2}, \end{aligned} \quad (45)$$

and

$$\begin{aligned}
\eta^{\text{TE}} &= \pm \sqrt{\frac{(1 + S_{11}^{\text{TE}})^2 - (S_{21}^{\text{TE}})^2}{(1 - S_{11}^{\text{TE}})^2 - (S_{21}^{\text{TE}})^2}} \sec \theta_i & \eta^{\text{TM}} &= \pm \sqrt{\frac{(1 + S_{11}^{\text{TM}})^2 - (S_{21}^{\text{TM}})^2}{(1 - S_{11}^{\text{TM}})^2 - (S_{21}^{\text{TM}})^2}} \sec \theta_i \\
n^{\text{TE}} &= \sqrt{\left[\frac{|\log|\zeta^{\text{TE}}| + j(\angle\theta^{\text{TE}})|}{-jk_0 d} \right]^2 + \sin^2 \theta_i} & n^{\text{TM}} &= \sqrt{\left[\frac{|\log|\zeta^{\text{TM}}| + j(\angle\theta^{\text{TM}})|}{-jk_0 d} \right]^2 + \sin^2 \theta_i} \\
\zeta^{\text{TE}} &= \frac{S_{21}^{\text{TE}}}{1 - S_{11}^{\text{TE}} \frac{\eta^{\text{TE}} \cos \theta_i - 1}{\eta^{\text{TE}} \cos \theta_i + 1}} & \zeta^{\text{TM}} &= \frac{S_{21}^{\text{TM}}}{1 - S_{11}^{\text{TM}} \frac{\eta^{\text{TM}} \cos \theta_i - 1}{\eta^{\text{TM}} \cos \theta_i + 1}}.
\end{aligned} \tag{46}$$

An example of parameter retrieval applied to ADLs is shown in Figure 25. A few consideration can be made on the results:

- The x and y -components of the permittivity tensor are equal ($\varepsilon_x = \varepsilon_y$). This is expected because the ADL geometry is the same along the x and y -directions;
- The z -component of the permittivity ε_z is equal to the permittivity of the host medium. This is expected since the z -component of the electric field is orthogonal to the metal and does not ‘see’ the patches;
- The permittivity is directly proportional to the shift between layers and inversely to the inter-layer distance;
- The x and y -components of the permeability tensor are equal to 1 ($\mu_x = \mu_y = 1$);
- The z -component of the permeability tensor $\mu_z < 1$ and inversely proportional to $\varepsilon_x, \varepsilon_y$;

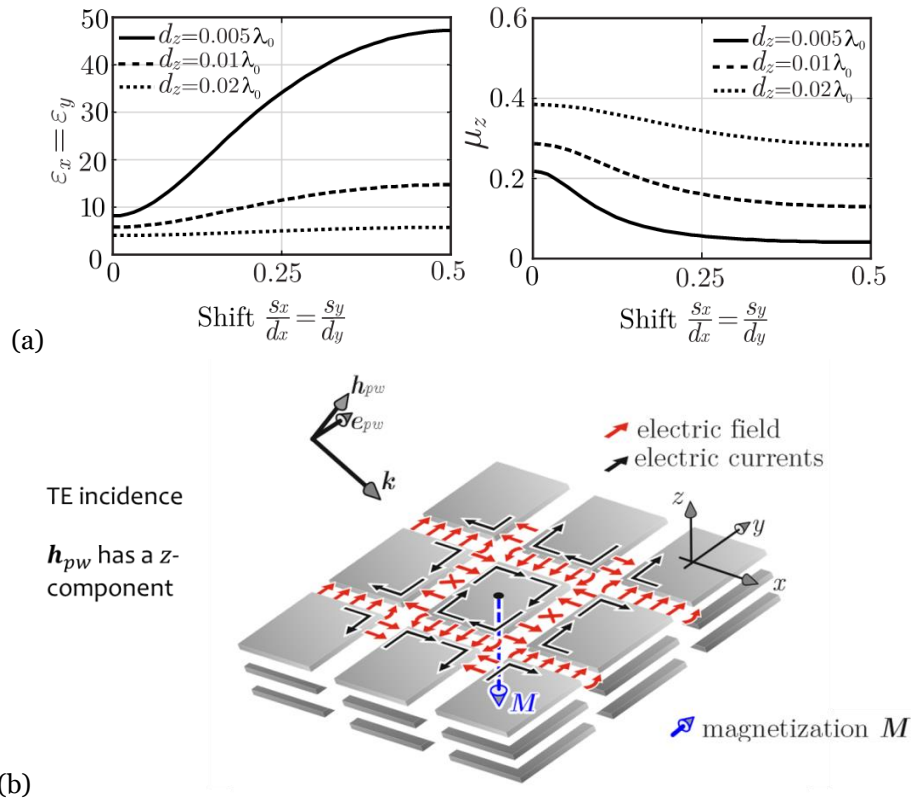


Figure 25. (a) Relevant components of the equivalent permittivity and permeability tensors for ADL and (b) field picture to explain the diamagnetism property.

A material with permeability lower than 1 is called diamagnetic. Real diamagnetic material that are found in nature are typically only slightly diamagnetic, with μ_r very close to 1 (e.g. $\mu_r = 0.9999$). ADLs realize a material that is artificially strongly diamagnetic. To understand why this is the case, Figure 25(b) presents a graphical interpretation of the diamagnetism of ADLs. In the case of TE incidence, for which the incident magnetic field has a nonzero z-component, the induced electric field distribution on a layer is compatible with loops of electric current on the metal patches. The loop currents produce a magnetic field (magnetization) opposite to the incident one. Therefore, the total magnetic field inside the ADL is reduced compared to the external one (i.e., $\mu_z < 1$).

4.2 Design Tool

The expressions given in these notes were implemented in a tool which is available on the website of the THz Sensing group at [18]. The graphical user interface (GUI) is shown in Figure 26. The tool allows you to fill in the geometrical parameters of a given artificial dielectric stratification and will give the following output:

- The equivalent refractive index, at broadside and as a function of incidence angle, for both TE and TM incidence;
- The range in which the electrical parameters will lie when tolerances are applied to various geometrical parameters;
- The components of the equivalent permittivity and permeability tensors;
- The equivalent electric and magnetic dissipation factors, due to the finite conductivity of the metal.

Although not currently implemented, the closed-form expressions for the ADLs are not only useful for the analysis (find effective electrical parameters from a given geometry), but also for the opposite problem of synthesis (find the geometry that gives certain desired electromagnetic properties). The synthesis is particularly useful for the engineering of ADLs with desired characteristics.

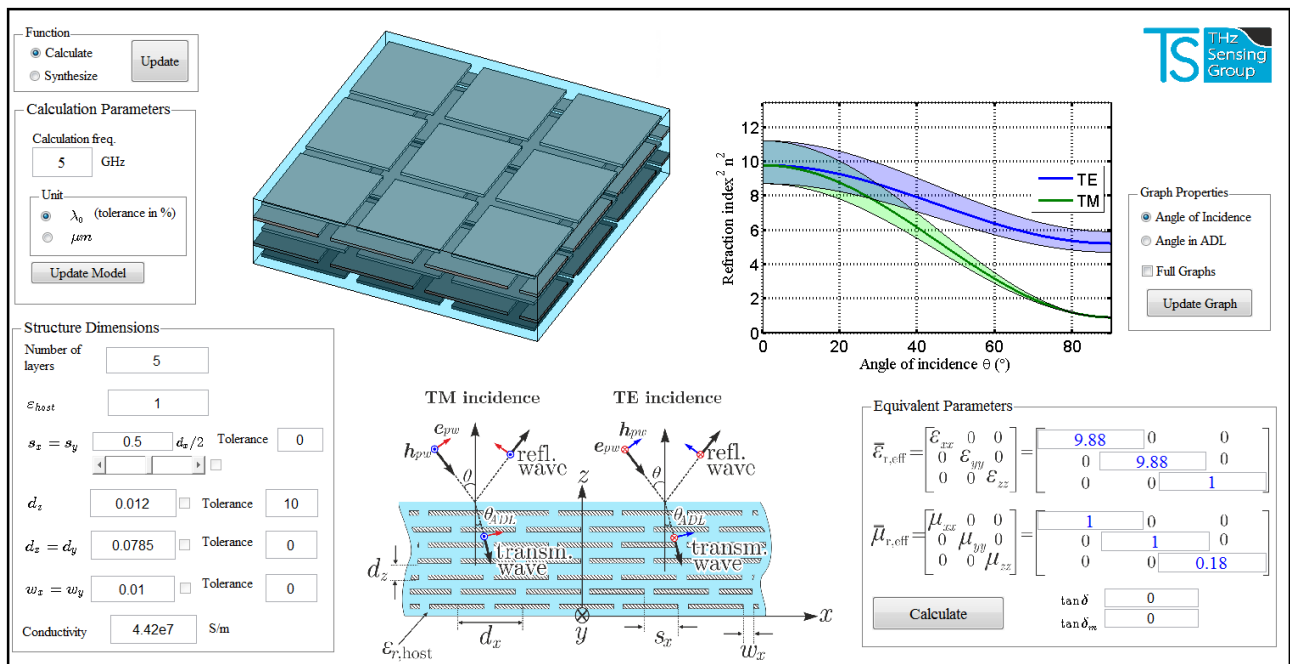


Figure 26. Graphical user interface of the ADL design tool.

References

- [1] W. E. Kock, "Metallic delay lenses," *Bell System Tech. J.*, vol. 27, no. 1, pp. 58-82, Jan. 1948.
- [2] S. S. D. Jones and J. Brown, "Metallic delay lenses," *Nature*, vol. 163, no. 4139, pp. 324-325, Feb. 1949.
- [3] R. E. Collin, *Field Theory of Guided Waves, 2nd Ed.* IEEE Press, New York, 1991.
- [4] W. H. Syed and A. Neto, "Front-to-back ratio enhancement of planar printed antennas by means of artificial dielectric layers," *IEEE Trans. Antennas Propag.*, vol. 61, no. 11, pp. 5408-5416, Nov. 2013.
- [5] W. H. Syed, G. Fiorentino, D. Cavallo, M. Spirito, P. M. Sarro, and A. Neto, "Design, fabrication and measurement of 0.3 THz on-chip double-slot antenna enhanced by artificial dielectrics," *IEEE Trans. THz Sci. Tech.*, vol. 5, no. 2, pp. 288-298, Mar. 2015.
- [6] D. Cavallo, W. H. Syed, and A. Neto, "Connected-slot array with artificial dielectrics: A 6 to 15 GHz dual-pol wide-scan prototype," *IEEE Trans. Antennas Propag.*, vol. 66, no. 6, pp. 3201-3206, Jun. 2018.
- [7] D. Cavallo, W. H. Syed, and A. Neto, "Closed-form analysis of artificial dielectric layers—Part I: Properties of a single layer under plane-wave incidence," *IEEE Trans. Antennas Propag.*, vol. 62, no. 12, pp. 6256-6264, Dec. 2014.
- [8] J. R. Wait, *Electromagnetic Scattering*. P.L.E. Uslenghi, Ed., Academic Press, Inc., 1978.
- [9] R. C. Compton and D. B. Rutledge, "Approximation techniques for planar periodic structures," *IEEE Trans. Microw. Theory Tech.*, vol. 33, no. 10, pp. 1083-1088, Oct. 1985.
- [10] O. Luukkonen et al., "Simple and accurate analytical model of planar grids and high-impedance surfaces comprising metal strips or patches," *IEEE Trans. Antennas Propag.*, vol. 56, no. 6, pp. 1624-1632, Jun. 2008.
- [11] S. A. Tretyakov, *Analytical Modelling in Applied EM*. Artech House, 2003.
- [12] D. Cavallo, W. H. Syed, and A. Neto, "Closed-form analysis of artificial dielectric layers—Part II: Extension to multiple layers and arbitrary illumination," *IEEE Trans. Antennas Propag.*, vol. 62, no. 12, pp. 6265-6273, Dec. 2014.
- [13] D. Cavallo, "Dissipation losses in artificial dielectric layers," *IEEE Trans. Antennas Propag.*, vol. 66, no. 12, pp. 7460-7465, Dec. 2018.
- [14] C. Felita and D. Cavallo, "Analytical formulas for artificial dielectrics with non-aligned layers," *IEEE Trans. Antennas Propag.*, vol. 65, no. 10, pp. 5303-5311, Oct. 2017.
- [15] A. Hessel, M. H. Chen, R. C. M. Li and A. A. Oliner, "Propagation in periodically loaded waveguides with higher symmetries," *Proc. IEEE*, vol. 61, no. 2, pp. 183-195, Feb. 1973.
- [16] W. H. Syed, D. Cavallo, H. Thippur Shivamurthy, and A. Neto, "Wideband, wide-scan planar array of connected slots loaded with artificial dielectric superstrates," *IEEE Trans. Antennas Propag.*, vol. 64, no. 2, pp. 543-553, Feb. 2016.
- [17] D. Cohen and R. Shavit, "Bi-anisotropic Metamaterials Effective Constitutive Parameters Extraction Using Oblique Incidence S-Parameters Method," *IEEE Trans. Antennas Propag.*, vol. 63, no. 5, pp. 2071-2078, May 2015.
- [18] <http://terahertz.tudelft.nl/Research/project.php?id=114&pid=81>